applied sciences

MDPI

Article

Sensitivity Analysis of Fracture Geometry Parameters on the Mechanical Behavior of Rock Mass with an Embedded Three-Dimensional Fracture Network

Na Wu [1], Zhengzhao Liang [1], Yan Tao [1], Ting Ai [2,*] and Guijie Li [3]

[1] State Key Laboratory of Coastal and Offshore Engineering, Dalian University of Technology, Dalian 116024, China
[2] Key Laboratory of Deep Earth Science and Engineering, Ministry of Education, Sichuan University, Chengdu 610065, China
[3] School of Aeronautics and Astronautics, Dalian University of Technology, Dalian 116024, China
* Correspondence: aiting@scu.edu.cn

Abstract: The existence of fractures has a significant influence on the mechanical properties of a rock mass. The sensitivity of the rock mass's mechanical properties to the fracture's geometric parameters is conducive to improving the measurement accuracy of fractured rock mass engineering. Firstly, the fracture geometric parameters in the dam site area of Lianghekou Hydropower Station were counted using the ShapeMetriX^{3D} system. Then, the effect of the fracture's geometric parameters on the deformation characteristics, failure mode, and mechanical parameters of the rock mass were investigated based on the RFPA^{3D} under the uniaxial compression test. The results showed that the stress–strain curves of the fractured rock mass mainly exhibited elastic-brittle characteristics. The failure pattern of the fractured rock mass was mainly defined by a compressive-shear composite. Additionally, the influence of the fracture's geometric parameters on the uniaxial compressive strength (UCS) was greater than that of elastic modulus. The sensitivity of the UCS to fracture trace length was more significant.

Keywords: fractured rock mass; ShapeMetriX^{3D} system; fracture geometric parameter; sensitivity analysis; failure mode

Citation: Wu, N.; Liang, Z.; Tao, Y.; Ai, T.; Li, G. Sensitivity Analysis of Fracture Geometry Parameters on the Mechanical Behavior of Rock Mass with an Embedded Three-Dimensional Fracture Network. *Appl. Sci.* **2022**, *12*, 9284. https://doi.org/10.3390/app12189284

Academic Editor: Arcady Dyskin

Received: 26 July 2022
Accepted: 14 September 2022
Published: 16 September 2022

1. Introduction

With the development of the social economy and the increase of national infrastructure investment, the scale and complexity of rock engineering have been increasing. The mechanical characteristics of the rock masses involved are becoming more and more complex. Rock masses differ from rocks in that they contain many discontinuous structural surfaces. Fractures are common discontinuities in rock masses [1,2] that intersect each other to form complex fracture networks. Fracture networks are an important reason for the extremely complex deformation characteristics of rock masses. The nonlinear, size effect, and anisotropic behavior of fractured rock masses are affected by their complex fracture networks [3,4]. The instability of rock masses is usually caused by the deformation, expansion, and penetration of the fractures in the fracture networks [5,6]. Additionally, the strength and deformation parameters are controlled by the complex fracture networks [7]. The complex fracture networks are usually determined by fracture geometry parameters, such as inclination, dip angle, and trace length of the fractures. Therefore, it is of great importance to study the influence of fracture geometry parameters on the mechanical properties of a rock mass.

Identifying and extracting fracture geometry information is essential for analyzing the mechanical and deformation properties of the fractured rock masses. There are two main ways to acquire a fracture's geometric information in an outcrop area, including

contact and non-contact measurements. The efficiency of contact measurement is lower, and the measurement accuracy cannot be guaranteed [8,9]. In recent years, non-contact measurement techniques (such as total station and photogrammetry) have been widely used to analyze fracture geometric information in a rock mass. It can effectively capture data from physically inaccessible areas [10]. Laser-scanning techniques are an effective non-contact measurement method. By analyzing the outcrop characteristics of visible fractures on the rock mass surface, point cloud data processing can be used to identify discontinuities and extract information from them [11]. A method to detect and estimate the orientation of plane structures was proposed based on the principal component analysis (PCA) techniques by Gomes et al. [12]. When applied to practical situations, it showed high precision in both the detection and location of fracture planes. A method for generating a high-resolution digital outcrop model (DOM) of the rock exposure based on UAV photogrammetry and the structural self-motion (SFM) technique was introduced and applied to slopes in Greece and China [13]. The results showed that UAV-SFM photogrammetry had higher efficiency and operability, especially in difficult measurement environments. Stereophotogrammetry is a method of extracting the regions of interesting information by constructing stereo images from two or more photographs. ShapeMetriX^{3D} is widely used for discerning the structural surface information statistics of rock slopes and tunnels [14–16]. The close-up photographs turned out useful to obtain detailed images and accurate results.

The distribution of fracture geometry parameters has certain statistical and probability distribution characteristics. Statistical methods are often used to quantitatively describe and analyze fracture geometry parameters. The fracture distribution function is obtained based on a fracture's geometry parameters and statistical methods [17,18]. The discrete fracture network (DFN) model provides an approach to characterize complex fractures based on the fracture distribution function [19]. The sizes, directions, spacings, and spatial locations of fractures are included in the DFN model. The DFN model is also an effective method to study the influence of fracture geometry parameters on the mechanical properties of complex fractured rock mass [20,21]. The model consists of the fractures embedded in the rock. For example, a stochastic DFN model was established based on the two-dimensional finite element method of rock failure process analysis (RFPA^{2D}). The failure modes, strength, and deformation parameters (elastic modulus and peak strength) of fractured rock mass were studied by Wu et al. [22]. Results showed that the fracture geometry parameters had a significant impact on the scale effect of the fractured rock mass. The effect of geometrical parameters of non-persistent fractures on the mechanical behaviors of the rock mass based on PFC^{2D} software was studied by Vaziri et al. [23] under uniaxial loading conditions. The results showed that the effect of random fractures on strength was greater than the effect of the deformation modulus. Amongst the fracture geometrical parameters, the fracture orientation had the most significant effect on the mechanical parameters of the rock mass.

The distribution of fractures in nature is three dimensional and spatial. A 3D equivalent DFN model was proposed based on the three-dimensional rock failure process analysis (RFPA^{3D}) software, and the scale effect and anisotropy of the fractured rock mass were analyzed by Wu et al. [24]. Moreover, the effects of the geometry (orientation, duration, spacing, aperture, and step angle) of parallel fractures on the uniaxial compressive strength (UCS) and deformation modulus were statistically investigated based on PFC^{3D} by Bahaaddini et al. [25]. It was found that the fracture orientation had the greatest influence on the UCS and deformation modulus, followed by the fracture spacing. However, the fractures in the model were not random, which was not consistent with the actual project. The effect of fracture geometry parameters on the equivalent mechanical parameters of the fractured rock mass based on the 3DEC software was studied by Cui et al. [26]. The results showed that the elastic modulus was the most sensitive to the structural density and the UCS was the most sensitive to the trace length of the fracture.

The estimation of the mechanical properties of fractured rock masses has always been a challenging task for practical rock engineers. A review of previous studies clearly showed that the fracture geometry parameters had a strong effect on the mechanical

behavior of rock mass. The DFN model is an effective method to study the mechanical behavior of rock masses. However, the DFN model relied heavily on the quality of natural fracture structural data gathered in the field. The purpose of this paper was to evaluate the influence of fracture geometry parameters on the mechanical properties of rock mass using a combination of finite element methods and a fracture network model. First, the ShapeMetriX^{3D} system was used to identify and extract the fracture geometry information in the dam site area of the Lianghekou Hydropower Station. The mean value, variance, and distribution types of fracture geometry parameters were obtained. Then, an orthogonal test scheme was designed based on the influencing factors and factor levels. The corresponding DFN models were established according to the fracture geometry parameters. The effects of fracture geometry parameters, including the inclination, dip angle, trace length and bulk density, on the UCS, elastic modulus, and failure pattern were studied under uniaxial loading conditions. Finally, the degree of influence of the fracture geometry parameters on the mechanical behavior of randomly fractured rock masses was statistically analyzed by using range analysis, variance analysis, and significance test.

2. Acquirement of Fracture Geometry Parameters

2.1. Research Background

The Lianghekou Hydropower Station is located on the main stream of the Yalong River in Yajiang County, Sichuan Province. The dam site is located about 2 km downstream of the confluence of the main stream of the Yalong River and the tributary of Xianshui River. The construction drawing in the dam site area of Lianghekou Hydropower Station is illustrated. The Yalong River flows north to south in the dam site area, crosses the IV exploration line, and returns to S23°E. It then flows from north to south again in the upper reaches of the unnamed ditch. The dam site is located in a lateral valley with a slope of 500–1000 m along the river edge. The left bank is curved and projects towards the right bank with an average topographic slope of 55° and multiple small gullies. The right bank is concave, with an average convex slope of 45°. The geological structure and tectonic environment of the Lianghekou reservoir area are generally simple. There are a few small faults, strong tectonic action, and no large-scale broken rock mass due to the intense tectonic action. The stability of the reservoir bank mainly depends on the stability degree of the existing landslide in the natural state, as well as any potential changes during reservoir storage.

The discontinuous surfaces of the slope rock mass, such as fissures and fractures, control the instability pattern of the slope. Therefore, the slope rock mass is weakened, and the safety of the engineering project is threatened. In this paper, the left bank side slope rock mass downstream of the dam site of Lianghekou Hydropower Station was studied, as shown in Figure 1.

Figure 1. Slope rock mass of the left bank near the dam site of the Lianghekou Hydropower Station.

The geometrical parameters in the fractures of the slope rock mass were counted by the 3D non-contact measurement system (ShapeMetriX^{3D} system). The influence law and sensitivity analysis of the fracture information on the mechanical properties of the fractured rock mass was conducted to provide reference data for the analysis of the slope instability. According to the investigation, the lithology of the rock mass in this area is metamorphic sandstone. The detailed mechanical parameters of the rocks and fractures are shown in Table 1.

Table 1. Mechanical parameters of the rocks and fractures in the study area [24,27].

Material Type	Heterogeneity	UCS/MPa	Elastic Modulus/GPa	Friction Angle/°	Poisson's Ratio
Rock	5	108.9	37.6	56	0.24
Fracture	2	5.45	1.88	30	0.39

2.2. Data Collection from the Study Area

The ShapeMetriX^{3D} system was produced by a 3GSM company in Austria. The system consists of a digital camera capable of calibrating 20 million high-resolution stereo images (Figure 2a), a software package for 3D model reconstruction and visualization analysis (Figure 2b), and a benchmark (Figure 2c). The specified area is imaged from two different angles, and the 3D geometric image is synthesized via technical processing to realize the real 3D model reconstruction of the solid surface.

(a) Digital camera

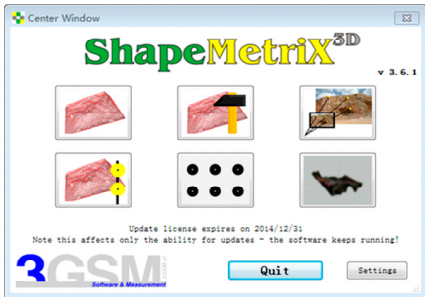

(b) ShapeMetriX^{3D} software

(c) Benchmark

Figure 2. Composition and principle of the ShapeMetriX^{3D} system. Research steps 1–5 are the process of data collection based on the equipment.

The steps to obtain the geometric information of 3D rock mass surface fractures are as follows: 1. Select an appropriate camera lens and set the camera parameters according to the working conditions of the shooting site. 2. Place the reference point in front of the test rock mass and make sure it is vertical. 3. Select two shooting points in front of the rock mass on the left and right to photograph the rock mass in the study area. The connection line between the two points is required to be parallel to the rock mass surface and meet the requirements of a certain distance. 4. Find an obvious structural plane on the rock mass surface and measure and record the tendency and inclination of the structural plane with a

geological compass. 5. Import the left and right pictures into the Shapemetrix^{3D} software separately, depict the research area, and synthesize. The 3D geometric images are generated. 6. The size and direction of the rock mass are corrected by the size of the benchmark and the inclination and dip angle of the selected structural plane for the reconstruction of a real 3D model of rock mass engineering. 7. The geometric information of the fracture surfaces is described quantitatively, the dominant groups of fracture surfaces are divided according to the production clustering, and the parameters of the production information of the fracture surfaces are obtained. There are three groups of fractures in the study area. The probability distributions and geometrical parameters of fracture groups are listed in Table 2. Refer to Wu et al. [24,27] for more details.

Table 2. Probability distribution and geometrical parameters of the fracture groups [24,27].

Material Type		1# Fracture Group	2# Fracture Group	3# Fracture Group
Inclination/°	Distribution type	Normal	Lognormal	Normal
	Mean value	235.15	351.34	94.73
	Standard deviation	6.48	0.15	13.68
Dip angle/°	Distribution type	Normal	Lognormal	Normal
	Mean value	25.98	28.16	85.80
	Standard deviation	8.41	0.83	9.92
Trace length/m	Distribution type	Lognormal	Normal	Lognormal
	Mean value	3.42	3.12	2.96
	Standard deviation	2.05	1.48	1.39
Spacing/m	Distribution type	Negative exponential	Lognormal	Negative exponential
	Mean value	1.35	1.70	0.69
	Standard deviation	1.21	1.55	0.7
Bulk density/m^{-3}	Mean value	0.01734	0.02020	0.05838

3. Orthogonal Test Scheme and Numerical Model

3.1. Orthogonal Test Scheme

The purpose of this paper was to study the effects of fracture inclination, dip angle, trace length, and bulk density (relating to spacing) on the UCS and elastic modulus of fractured rock masses. Due to a large number of influencing factors and levels, it is quite troublesome to calculate the scheme. The orthogonal test method can not only effectively reduce the workload of calculation, but also obtain satisfactory sample results [28,29]. As a result, an orthogonal test scheme with four influencing factors and three levels was selected, and $L_9(3^4)$ was chosen as the orthogonal table for the design of this test scheme, as shown in Table 3. There are nine group test protocols in the table. The column number indicates the test factor, while the value under that column number indicates the level used for that factor. The level values of each influencing factor based on the range of the main influence factors also are given in Table 3. The level values of the influencing factors of inclination are 47.24°, 94.49°, and 141.73°, respectively. To dip the angle, trace length, and bulk density, the level values were 28.60°, 57.20°, 85.80°, 0.987 m, 1.973 m, 2.960 m, 0.05838 m^{-3}, 0.07784 m^{-3}, and 0.09730 m^{-3} in the order of levels 1, 2, and 3. Therefore, the test protocols for each main control factor were established based on the orthogonal test scheme.

Table 3. Orthogonal arrays $L_9(3^4)$ of the test scheme.

Test Number	Influencing Factors			
	Inclination/°	Dip Angle/°	Trace Length/m	Bulk Density/m^{-3}
T-1	Level 1 (47.24)	Level 1 (28.60)	Level 1 (0.987)	Level 1 (0.05838)
T-2	Level 1	Level 2 (57.20)	Level 2 (1.973)	Level 2 (0.07784)
T-3	Level 1	Level 3 (85.80)	Level 3 (2.960)	Level 3 (0.09730)

Table 3. *Cont.*

Test Number	Influencing Factors			
	Inclination/°	Dip Angle/°	Trace Length/m	Bulk Density/m^{-3}
T-4	Level 2 (94.49)	Level 1	Level 2	Level 3
T-5	Level 2	Level 2	Level 3	Level 1
T-6	Level 2	Level 3	Level 1	Level 2
T-7	Level 3 (141.73)	Level 1	Level 3	Level 2
T-8	Level 3	Level 2	Level 1	Level 3
T-9	Level 3	Level 3	Level 2	Level 1

3.2. The Principle of RFPA^{3D}

A finite element software, RFPA^{3D} (three-dimensional realistic failure process analysis), was applied for the numerical simulation. RFPA^{3D} is an effective method based on the damage mechanics and the statistical theory to simulate the gradual failure process of rock mass. It is worth mentioning that the mechanical parameters (such as the strength and elastic modulus) of the model elements obey the Weibull distribution. Therefore, the distribution characteristics of a rock's mechanical parameters at the mesoscopic level can be considered in the RFPA^{3D}. Additionally, the macroscopic failure is the accumulation process of mesoscopic element failure. For detailed information on the calculational principles and model validity of the RFPA^{3D} software, please refer to papers [24,30,31]. The constitutive equations of the RFPA^{3D} software are briefly summarized in this section.

The elastic-brittle damage constitutive model was introduced into the RFPA^{3D} to describe the stress–strain relationship. The constitutive relationship of the model is expressed as follows:

$$\sigma = E\varepsilon = E_0(1 - D)\varepsilon \tag{1}$$

where σ and ε are the stress applied to the model and the corresponding strain, respectively; E represents the elastic modulus of the damaged element; and E_0 and D denote the initial elastic modulus of the element and the damage variable, respectively. However, with increasing load, the elastic modulus of the element degrades gradually with the increase of the D.

When the model element is in a uniaxial tension state, the maximum tensile strain criterion and the Mohr Coulomb criterion were used in the RFPA^{3D}. The corresponding D was defined as in Equation (2).

$$D = \begin{cases} 0 & \varepsilon > \varepsilon_{to} \\ 1 - \frac{\sigma_{\mathrm{rt}}}{\varepsilon E_0} & \varepsilon_{to} \geq \varepsilon \geq \varepsilon_{tu} \\ 1 & \varepsilon < \varepsilon_{tu} \end{cases} \tag{2}$$

where σ_{rt} denotes the residual stress of the model element, and $\sigma_{\mathrm{rt}} = \lambda\sigma_{\mathrm{t}}$. Among them, σ_{t} and λ are the tension stress applied on the model and the residual coefficient, respectively; ε_{to} is the failure strain threshold, which is the tensile strain corresponding to the elastic limit; ε_{tu} is the ultimate tensile strain coefficient, and $\varepsilon_{tu} = \eta\varepsilon_{to}$; η denotes the ultimate strain coefficient.

According to the elastic damage theory, the stress–strain relationship can be derived as follows:

$$\sigma_{ij} = \begin{cases} 2G\varepsilon_{ij} + \lambda\delta_{ij}\varepsilon_{kk} & \bar{\varepsilon} > \varepsilon_{to} \\ \frac{\sigma_{rt}}{\bar{\varepsilon}E_0}\left(2G\varepsilon_{ij} + \lambda\delta_{ij}\varepsilon_{kk}\right) = \frac{\sigma_{rt}}{\bar{\varepsilon}}\left(\frac{\varepsilon_{ij}}{1+\nu} + \frac{\delta_{ij}\varepsilon_{kk}}{(1+\nu)(1-2\nu)}\right) & \varepsilon_{to} \geq \bar{\varepsilon} \geq \varepsilon_{tu} \\ 0 & \bar{\varepsilon} < \varepsilon_{tu} \end{cases} \tag{3}$$

where G and ν are the shear modulus and the Poisson's ratio of the model element, respectively; when $i = j$, $\delta_{ij} = 1$; otherwise, $\delta_{ij} = 0$.

Moreover, the Mohr–Coulomb criterion is applied when the model element is in a uniaxial compression state. Similarly, the D is expressed as follows:

$$D = \begin{cases} 0 & \varepsilon_1 < \varepsilon_{co} \\ 1 - \frac{\sigma_{rc}}{\varepsilon_1 E_0} & \varepsilon_1 \geq \varepsilon_{co} \end{cases} \tag{4}$$

where σ_{co} and σ_{rc} are the initial and residual UCS of the model element, respectively, and $\sigma_{rc} = \lambda\sigma_{co}$, ε_1, and ε_{co} denote the maximum principal stress and the compressive strain threshold, respectively.

Similarly, the corresponding the stress–strain relationship can be written as follows:

$$\sigma_{ij} = \begin{cases} 2G\varepsilon_{ij} + \lambda\delta_{ij}\varepsilon_{kk} & \varepsilon_1 < \varepsilon_{co} \\ \frac{\sigma_{rc}}{\varepsilon_1 E_0}\left(2G\varepsilon_{ij} + \lambda\delta_{ij}\varepsilon_{kk}\right) = \frac{\sigma_{rc}}{\varepsilon_1}\left(\frac{\varepsilon_{ij}}{1+\nu} + \frac{\delta_{ij}\varepsilon_{kk}}{(1+\nu)(1-2\nu)}\right) & \varepsilon_1 \geq \varepsilon_{co} \end{cases} \tag{5}$$

3.3. Model Establishment Based on RFPA^{3D}

The sensitivity of fracture geometrical parameters to the elastic modulus and UCS of the fractured rock mass was investigated in the sloping rock of the Lianghekou Hydropower Station dam site. However, only the geometric parameters of the 3# fracture group changed during the study. The geometric parameters of the 1# and 2# fracture groups remained unchanged.

The model size of 10 m × 10 m × 10 m and the element number of 120 × 120 × 120 were chosen to build the equivalent rock mass DFN model based on the RFPA^{3D} software [30]. The input mechanical parameters of the RFPA software are the mesoscopic parameters of rock mass, which is related to the element size to reduce the mesh effect of the model. Nine numerical models of the orthogonal arrays of the test scheme were generated based on Tables 1 and 3, as shown in Figure 3. The red lines in the numerical model represent the intersections of the fractures and the rocks.

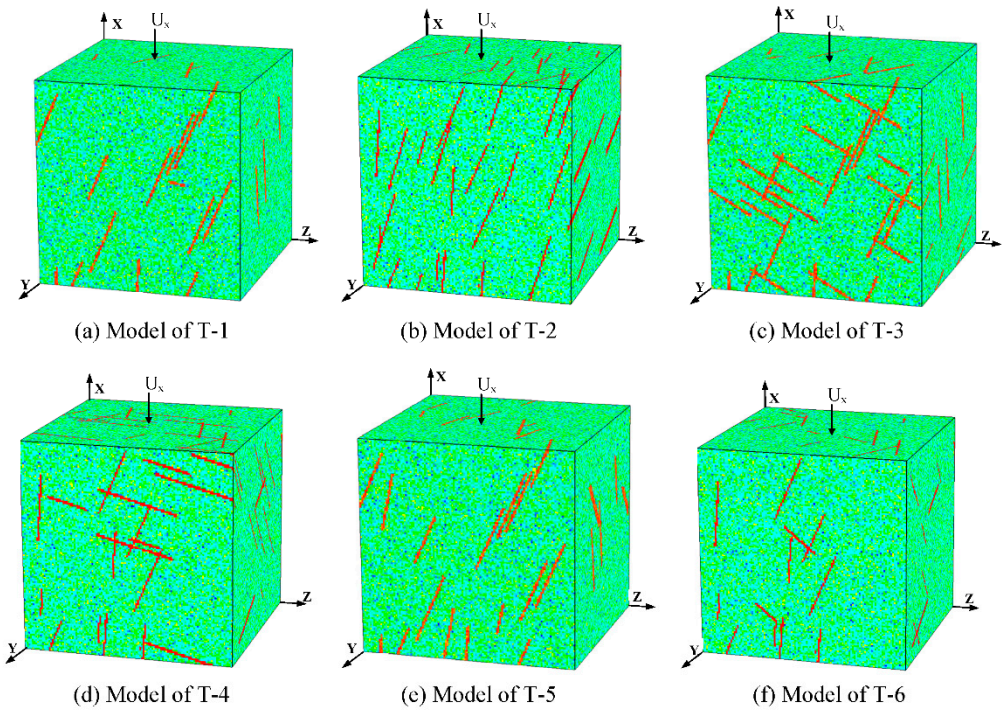

(a) Model of T-1 (b) Model of T-2 (c) Model of T-3

(d) Model of T-4 (e) Model of T-5 (f) Model of T-6

Figure 3. *Cont.*

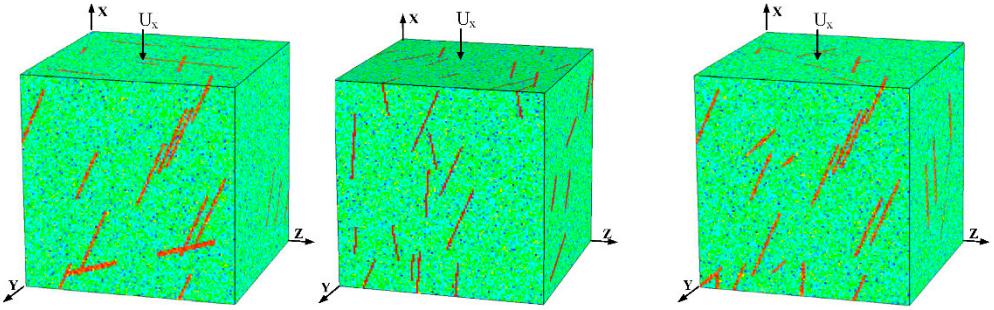

Figure 3. Numerical model of the orthogonal arrays of the test scheme.

Uniaxial, quasi triaxial, and true triaxial compression test of fractured rock mass can be implemented and simulated based on the RFPA3D software. However, the confining pressure may make the calculation results more complicated and diverse. To understand the sensitivity of the mechanical parameters of rock mass to geometric parameters under simple conditions, only the uniaxial compression test was adopted in this section.

During the simulation, the mechanical parameters and boundary conditions were kept constant during the tests except for the factors considered to enhance the reliability of the conclusions. The bottom surface (YOZ) of the model was fixed, and a displacement load (0.2 mm/step) was applied to the upper surface of the model parallel to the X-axis direction until the model failed. The remaining boundaries of the model are free.

4. Results and Analysis

4.1. Deformation Characteristics and Failure Patterns of Numerical Model

The stress–strain curves of the simulation results of the test scheme in Table 3 are shown in Figure 4. The results showed that the fractured rock mass presented brittle deformation, except for T-5, which exhibited elastic–plastic deformation. The deformation characteristics and failure pattern of test number T-1 in Table 3 were investigated as an example, as shown in Figure 5. The numerical model of the case is given in Figure 5a. The X-displacement diagram of the failure fractured rock mass is presented in Figure 5b. Red and blue colors represent the maximum and minimum deformation of the model, respectively. The deformation of the fractured rock mass in the *X*-axis direction was greatly influenced by DFN, and clear boundaries were formed at the intersections of the fractures and the rock. The deformation or displacement diagram of fractured rock mass decreased from top to bottom in the *X*-axis direction. Figure 5c shows the acoustic emission diagram of the failure model. Red circles in the acoustic emission diagram represent the damage events induced by compressive under the current load. In Figure 5d, the damage diagram of the failure model is plotted. The results showed that the fractured rock mass was mainly damaged along the fracture surface under the action of the external load. Due to the damage and failure of the fracture, multiple penetration shear faces were generated. The fractured rock mass was primarily defined by compressive-shear composite failure.

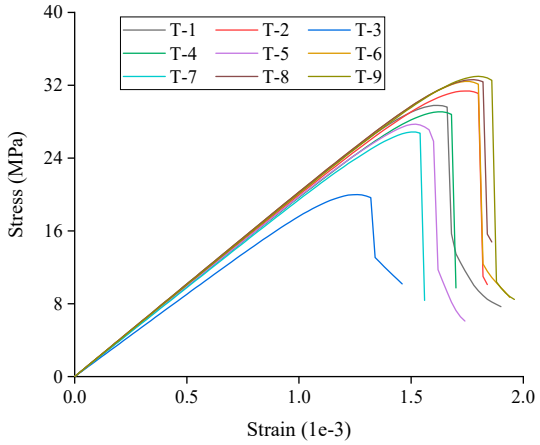

Figure 4. Stress–strain curves of the numerical models.

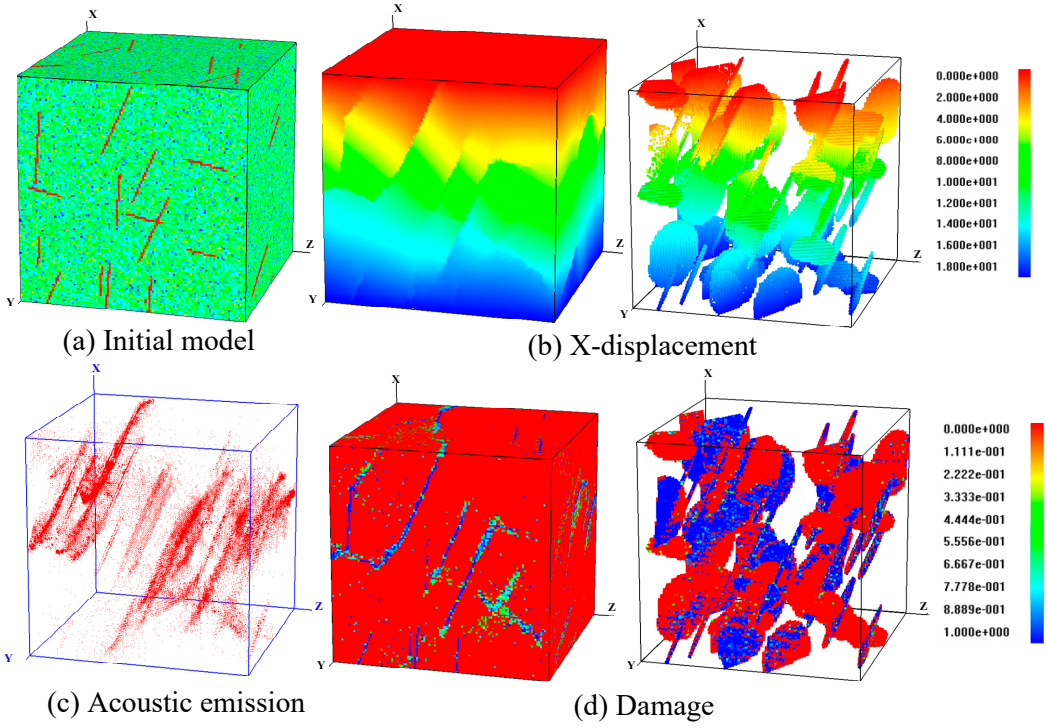

Figure 5. The deformation characteristics and failure pattern for T-1.

4.2. Strength and Deformation Parameters

Meanwhile, the elastic modulus and UCS of the models could be acquired based on the stress–strain curves. The elastic modulus is the slope of the line part of the stress–strain curve in the elastic stage. The UCS is the peak strength in the stress–strain curve. The elastic modulus and UCS provide parameters for sensitivity analysis.

Table 4 lists the test assignment scheme and the numerical results for each factor level based on the orthogonal table of the test scheme. The order of the test scenarios is consistent with Table 3. The values of each influencing factor, and the corresponding elastic modulus and UCS derived from numerical simulation under different schemes are also presented in Table 5. The results showed that the variations in fracture inclination, dip angle, trace length, and bulk density had significant effects on the elastic modulus and UCS of the fractured rock mass.

Table 4. The elastic modulus and UCS under various influencing factors and levels.

Test Number	Influencing Factors				Numerical Results	
	Inclination/°	Dip Angle/°	Trace Length/m	Bulk Density/m^{-3}	Elastic Modulus /GPa	UCS/MPa
T-1	47.24	28.60	1.48	0.029	20.362	29.794
T-2	94.49	28.60	2.96	0.058	20.063	31.378
T-3	141.73	28.60	4.44	0.0871	18.114	19.996
T-4	47.24	57.20	2.96	0.087	19.807	29.094
T-5	94.49	57.20	4.44	0.029	19.881	27.730
T-6	141.73	57.20	1.48	0.058	20.351	32.415
T-7	47.24	85.80	4.44	0.058	19.572	26.869
T-8	94.49	85.80	1.48	0.087	20.356	32.609
T-9	141.73	85.80	2.96	0.029	20.173	32.977

Table 5. Level values of the influencing factors of the Group 2 test.

Influencing Factors	Level 1	Level 2	Level 3
Inclination/°	47.24	94.49	141.73
Dip angle/°	28.60	57.20	85.80
Trace length/m	1.974	3.948	5.92
Bulk density/m^{-3}	0.05838	0.07784	0.09730

4.3. Range Analysis

Range analysis, also known as visual analysis, is one of the most common methods used to analyze the result of orthogonal tests. The problem is analyzed by the difference between the maximum and minimum in the mean effect. The specific formula is as follows:

$$R_i = \max\{k_{i1}, k_{i2}, \cdots, k_{ij}\} - \min\{k_{i1}, k_{i2}, \cdots, k_{ij}\} \quad (6)$$

where k_{ij} presents the mean value of the test results of the i influencing factor on the j level. R_i is refers to the extreme difference in the value of the influencing factor of i, that is, the difference between the maximum and minimum values of the test results at each level of the i influencing factor. The value reflects the variation range in the test results when the influencing factor of i changes. The larger the value of R, the greater the influence of the factor on the overall experiment results, which is a major influence. Conversely, it has a small effect.

Figure 6 shows the data analysis of the influencing factor level on the elastic modulus and UCS, respectively. The results showed that the influence degree of the four influencing factors on the elastic modulus of the fractured rock mass was in the order of track length, bulk density, dip angle, and inclination. However, for the UCS, the track length, inclination, bulk density, and dip angle were arranged in descending order. Therefore, the fracture trace length based on the extreme difference analysis was the main factor affecting the elastic modulus of the fractured rock mass and UCS.

The range analysis is easier to calculate and can prioritize the effect of factors on the calculated results. However, it is impossible to determine whether the influencing factors of the experiment are significant. Furthermore, errors are inevitable during the experiment, and range analysis makes it difficult to distinguish whether the differences corresponding to each factor level are due to experimental error or the factor level itself.

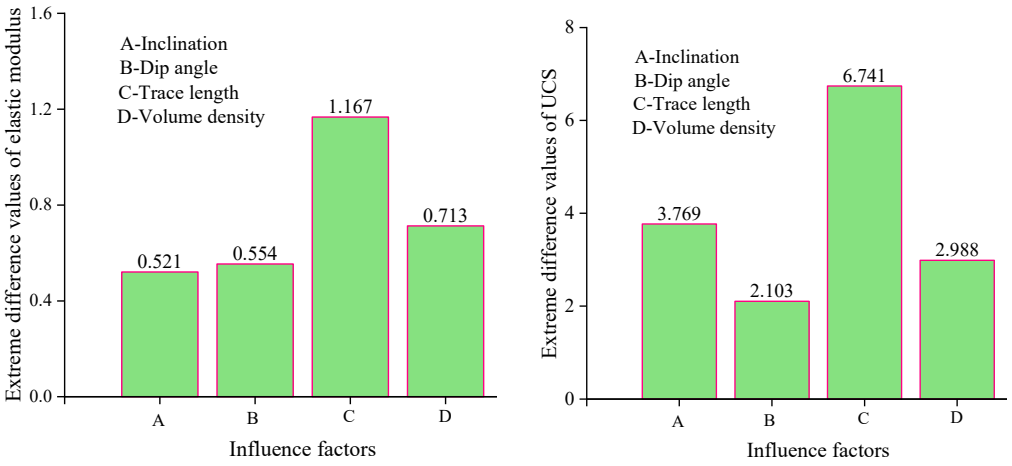

Figure 6. Extreme difference values of the elastic modulus and UCS under various influencing factors.

4.4. Variance Analysis and Significance Test

Variance analysis is widely used in data processing of the orthogonal test and can compensate for the deficiencies of the range analysis. The corresponding sum of squared variance and sum of squared errors need to be calculated for the experiment data when the variance analysis is applied. Based on the calculation results of the elastic modulus and UCS at different influencing factor levels in the orthogonal test, the corresponding sums of deviations squares, errors squares, and degrees of freedom for each factor were calculated with the help of an orthogonal design assistant. Moreover, the mean square is the ratio of the sum of squares of deviation to the degree of freedom. The F ratio is the ratio of the mean square of each factor to the mean square of error, respectively. Therefore, the mean square and the F ratio of each factor could be calculated for the elastic modulus and UCS, as shown in Figure 7. Finally, the F-ratios were compared with the critical values of $F_{0.01}(2,\ 6)$ and $F_{0.05}(2,\ 6)$. If $F > F_{0.01}(2,\ 6)$, the factor was highly significant, denoted by **. If $F_{0.01}(2,\ 6) > F > F_{0.05}(2,\ 6)$, the factor was significant, denoted by *. If $F < F_{0.05}(2,\ 6)$, the factor was highly insignificant. Among them, $F_{0.01}(2,\ 6) = 10.93$ and $F_{0.05}(2,\ 6) = 5.14$.

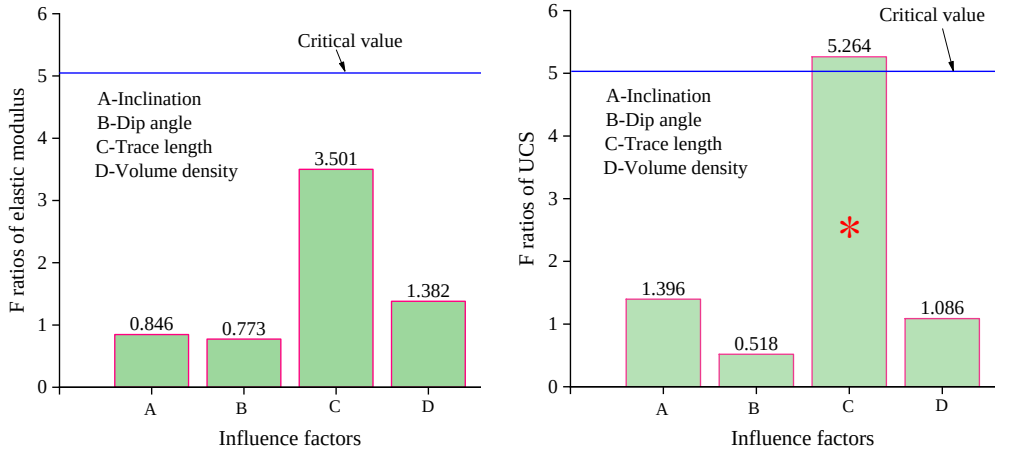

Figure 7. F ratio and significance levels of the elastic modulus and UCS under various influencing factors.

As shown in Figure 7, the results demonstrated that the sensitivity of the rock mass elastic modulus to the four influencing factors was not significant. The main reason is that the elastic modulus is an inherent characteristic of the rock mass, which is mainly related to the chemical composition of material and not its structural state. Besides, the sensitivity of the rock mass elastic modulus to the four influencing factors was in the order of trace

length > bulk density > inclination > dip angle. The sensitivity analysis of rock mass UCS to the trace length of fracture was significant, while the sensitivity analysis to the inclination, dip angle, and bulk density of the fracture was insignificant. The sensitivity degree of the rock mass UCS to the four influencing factors was in the order of trace length > inclination > bulk density > dip angle, which is also consistent with the results of the range analysis.

5. Discussion

From the abovementioned research, it could be found that the effect of the fracture on the UCS was greater than the elastic modulus, which is consistent with the results of Vaziri et al. [23]. Additionally, the mechanical parameters of the fractured rock mass were sensitive to the fracture traces, which is in agreement with Cui and Sheng [26]. However, Vaziri et al. [23] and Bahaaddini et al. [24] found that fracture orientation was the most effective parameter among the fracture geometrical parameters, which is inconsistent with the results of this paper. The main reason could be that the fractured rock mass was generated based on a 2D PFC and the fracture orientation (dip angle) was considered in 2D space by Vaziri et al. [23]. Moreover, although a three-dimensional numerical model was applied by Bahaaddini et al. [25], the fractures in the rock mass were assumed to be parallel and only the fracture orientation (dip angle) was changed in the calculation results. Fractures in the rock mass are three-dimensional and their orientation is determined by the inclination and dip angle.

Additionally, the geometric parameters involved in this research do not completely exactly agree with those of other authors. The sensitivity orders of the rock mass mechanical parameters to the rock mass geometry parameters were also different from other authors. To increase the credibility of the conclusions, another orthogonal test was performed. The study methodology, test scheme, and analysis method are consistent with parts III and IV of the paper. Only the level values of the trace length were changed, as shown in Table 5.

The specific calculation results are not described in detail here. Extreme differences and F ratios of the elastic modulus and UCS for various influencing factors in the Group 2 test are presented in Figure 8. The results showed that the influence of the fracture geometry parameters in the UCS was greater than that of the elastic modulus. The results are consistent with the results of the Group 1 test.

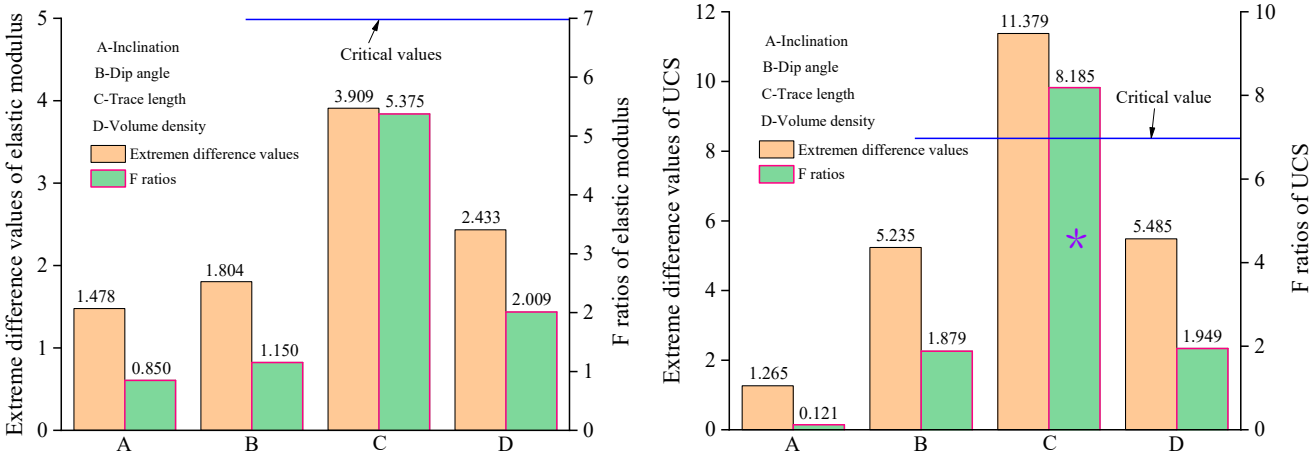

Figure 8. Extreme difference values and F ratios under various influencing factors of the Group 2 test.

Besides, in the Group 2 test, the sensitivity degree of the rock mass elastic modulus and UCS to the four influencing factors was in the order of trace length > bulk density > dip angle > inclination, which are different than the results of the Group 1 test. Therefore, when the influencing factors take different data in the range of values, the order of the sensitivity of the rock mass mechanical parameters to the fracture geometry parameters may be different. To fully understand the problem, the global sensitivity analysis method

can be used [32,33]. The Monte Carlo method was applied in the global sensitivity analysis method to generate a random set of data over a reasonable range of parameters to determine the influencing factors. The parameters of different influencing factors were then combined to establish a numerical model and acquire results. Generally, hundreds or even thousands of time-valued simulations are required.

6. Conclusions

The fracture geometry parameters and distribution types of the downstream slope of the left bank of the Lianghekou Hydropower Station were acquired based on the ShapeMetriX3D system. The sensitivity of rock mass mechanical parameters to the 3# group of the fracture geometry parameters was investigated according to the orthogonal test scheme. Moreover, the RFPA3D software was applied.

The behavior characteristics and failure pattern of the fractured rock mass were analyzed. The results showed that the stress–strain curve of the fractured rock mass mainly exhibited an elastic-brittle behavior. The macroscopic failure mode of fractured rock mass is a compressive-shear composite failure pattern.

Range analysis, variance analysis, and significance test were used to analyze the sensitivity of the fractured rock mass mechanical parameters to the fracture geometry. The results indicated that the influence of the fracture geometry parameters in the UCS was greater than that of elastic modulus. The sensitivity of the UCS to fracture trace length was significant, but not to the bulk density, dip angle, and inclination of fracture. The elastic modulus of the fractured rock mass was insensitive to the fracture geometrical parameters.

The research results provide a reference for the measurement and statistics of fracture geometrical parameters in the engineering rock mass, as well as improving the accuracy of the analysis of the mechanical parameters of a fractured rock mass.

Author Contributions: Conceptualization, Z.L.; methodology, N.W.; software, Z.L.; formal analysis, N.W.; investigation, Y.T.; resources, N.W.; data curation, N.W.; writing—original draft preparation, N.W.; writing—review and editing, G.L.; supervision, Z.L.; project administration, T.A.; funding acquisition, Z.L. and T.A. All authors have read and agreed to the published version of the manuscript.

Funding: This research was funded by the National Natural Science Foundation of China (Grant No. 52209123), Open Fund of Key Laboratory of Deep Earth Science and Engineering (Sichuan University), Basic Scientific Research Projects of Dalian University of Technology (DUT21RC(3)071).

Institutional Review Board Statement: Not applicable.

Informed Consent Statement: Not applicable.

Data Availability Statement: Not applicable.

Acknowledgments: The authors thank the anonymous reviewers, who provided valuable suggestions that improved the manuscript.

Conflicts of Interest: The authors declare no conflict of interest.

List of Symbols

U_x	A displacement load parallel to the X-axis direction
k_{ij}	The mean value of test results of the influencing factor (i) on the level (j).
R_i	The extreme difference in the value of the influencing factor of i.
$F_\alpha(x,\ y)$	F-value with a significant level of α, number of independent variables as x and degrees of freedom as y.

References

1. Mu, W.Q.; Wang, D.Y.; Li, L.C.; Yang, T.H.; Feng, Q.B.; Wang, S.X.; Xiao, F.K. Cement Flow in Interaction Rock Fractures and its Corresponding New Construction Process in Slope Engineering. *Constr. Build. Mater.* **2021**, *303*, 124533. [CrossRef]
2. Gong, B.; Wang, Y.Y.; Zhao, T.; Tang, C.A.; Yang, X.Y.; Chen, T.T. AE Energy Evolution during CJB Fracture Affected by Rock Heterogeneity and Column Irregularity under Lateral Pressure. *Geomat. Nat. Haz. Risk.* **2022**, *13*, 877–907. [CrossRef]

3. Liang, Z.Z.; Wu, N.; Li, Y.C.; Li, H.; Li, W.R. Numerical Study on Anisotropy of the Representative Elementary Volume of Strength and Deformability of Jointed Rock Masses. *Rock Mech. Rock Eng.* **2019**, *52*, 4387–4402. [CrossRef]
4. Wu, N.; Liang, Z.Z.; Li, Y.C.; Li, H.; Li, W.R.; Zhang, M.L. Stress-Dependent Anisotropy Index of Strength and Deformability of Jointed Rock Mass: Insights from a Numerical Study. *Bull. Eng. Geol. Environ.* **2019**, *78*, 5905–5917. [CrossRef]
5. Qiu, L.; Zhu, Y.; Song, D.; He, X.; Wang, W.; Liu, Y.; Xiao, Y.; Wei, M.; Yin, S.; Liiu, Q. Study on the Nonlinear Characteristics of EMR and AE during Coal Splitting Tests. *Minerals* **2022**, *12*, 108. [CrossRef]
6. Strauhal, T.; Zangerl, C. The Impact of Fracture Persistence and Intact Rock Bridge Failure on the In Situ Block Area Distribution. *Appl. Sci.* **2021**, *11*, 3973. [CrossRef]
7. Bonilla-Sierra, V.; Scholtès, L.; Donzé, F.V.; Elmouttie, M.K. Rock Slope Stability Analysis Using Photogrammetric Data and DFN–DEM Modelling. *Acta Geotech.* **2015**, *10*, 497–511. [CrossRef]
8. Li, X.; Chen, Z.; Chen, J.; Zhu, H. Automatic Characterization of Rock Mass Discontinuities Using 3D Point Clouds. *Eng. Geol.* **2019**, *259*, 105131. [CrossRef]
9. Lato, M.J.; Diederichs, M.S.; Hutchinson, D.J. Bias Correction for View-Limited Lidar Scanning of Rock Outcrops for Structural Characterization. *Rock Mech. Rock Eng.* **2010**, *43*, 615–628. [CrossRef]
10. Otoo, J.N.; Maerz, N.H.; Li, X.; Duan, Y. Verification of a 3-D LiDAR Viewer for Discontinuity Orientations. *Rock Mech. Rock Eng.* **2013**, *46*, 543–554. [CrossRef]
11. Pan, D.D.; Li, S.C.; Xu, Z.H.; Zhang, Y.C.; Lin, P.; Li, H.Y. A Deterministic-Stochastic Identification and Modelling Method of Discrete Fracture Networks Using Laser Scanning: Development and Case Study. *Eng. Geol.* **2019**, *262*, 105310. [CrossRef]
12. Gomes, R.K.; de Oliveira, L.P.L.; Gonzaga, L.; Tognoli, F.M.W.; Veronez, M.R.; de Souza, M.K. An Algorithm for Automatic Detection and Orientation Estimation of Planar Structures in LiDAR-Scanned Outcrops. *Comput. Geosci.* **2016**, *90*, 170–178. [CrossRef]
13. Kong, D.; Saroglou, C.; Wu, F.; Sha, P.; Li, B. Development and Application of UAV-SfM Photogrammetry for Quantitative Characterization of Rock Mass Discontinuities. *Int. J. Rock Mech. Min.* **2021**, *141*, 104729. [CrossRef]
14. Cho, J.W.; Jeon, S.; Jeong, H.Y.; Chang, S.-H. Evaluation of Cutting Efficiency during TBM Disc Cutter Excavation within a Korean Granitic Rock Using Linear-Cutting-Machine Testing and Photogrammetric Measurement. *Tunn. Undergr. Sp. Technol.* **2013**, *35*, 37–54. [CrossRef]
15. Sharif, L.K.; Elmo, D.; Stead, D. Improving DFN-Geomechanical Model Integration Using a Novel Automated Approach. *Comput. Geosci.* **2019**, *105*, 228–248.
16. Buyer, A.; Aichinger, S.; Schubert, W. Applying Photogrammetry and Semi-Automated Joint Mapping for Rock Mass Characterization. *Eng. Geol.* **2020**, *264*, 105332. [CrossRef]
17. Yang, T.H.; Wang, P.T.; Xu, T.; Yu, Q.L.; Zhang, P.H.; Shi, W.H.; Hu, G.J. Anisotropic Characteristics of Jointed Rock Mass: A Case Study at Shirengou Iron Ore Mine in China. *Tunn. Undergr. Sp. Technol.* **2015**, *48*, 129–139. [CrossRef]
18. Ma, G.W.; Li, M.Y.; Wang, H.D.; Chen, Y. Equivalent Discrete Fracture Network Method for Numerical Estimation of Deformability in Complexly Fractured Rock Masses. *Eng. Geol.* **2020**, *277*, 105784. [CrossRef]
19. Ren, F.; Ma, G.W.; Fan, L.F.; Wang, Y.; Zhu, H.H. Equivalent Discrete Fracture Networks for Modelling Fluid Flow in Highly Fractured Rock Mass. *Eng. Geol.* **2017**, *229*, 21–30. [CrossRef]
20. Miyoshi, T.; Elmo, D.; Rogers, S. Influence of Data Analysis When Exploiting DFN Model Representation on the Application of Rock Mass Classification Systems. *J. Rock Mech. Geotech.* **2018**, *10*, 1046–1062. [CrossRef]
21. Pakzad, R.; Wang, S.; Sloan, S. Numerical Study of the Failure Response and Fracture Propagation for Rock Specimens with Preexisting Flaws under Compression. *Int. J. Geomech.* **2018**, *18*, 04018070. [CrossRef]
22. Wu, N.; Liang, Z.Z.; Li, Y.C.; Qian, X.K.; Gong, B. Effect of Confining Stress on Representative Elementary Volume of Jointed Rock Masses. *Geomech. Eng.* **2019**, *18*, 627–638.
23. Vaziri, M.R.; Tavakoli, H.; Bahaaddini, M. Statistical Analysis on the Mechanical Behaviour of Non-Persistent Jointed Rock Masses Using Combined DEM and DFN. *B. Eng. Geol. Environ.* **2022**, *81*, 177. [CrossRef]
24. Wu, N.; Liang, Z.Z.; Zhang, Z.H.; Li, S.H.; Lang, Y.X. Development and Verification of Three-Dimensional Equivalent Discrete Fracture Network Modelling Based on the Finite Element Method. *Eng. Geol.* **2022**, *306*, 106759. [CrossRef]
25. Bahaaddini, M.; Hagan, P.; Mitra, R.; Hebblewhite, B.K. Numerical Study of the Mechanical Behavior of Nonpersistent Jointed Rock Masses. *Int. J. Geomech.* **2016**, *16*, 04015035. [CrossRef]
26. Cui, Z.; Sheng, Q. Numerical Modelling of Structural Effect of Equivalent Mechanical Parameters of Fractured Rock Mass. *Rock Soil Mech.* **2018**, *39*, 3830–3841.
27. Wu, N.; Liang, Z.Z.; Song, W.C.; Li, W.R. Construction of a 3D Equivalent Rock Random Fracture Network Model and its Application in the Lianghekou Hydropower Station. *Chin. J. Eng.* **2022**, *44*, 1282–1290.
28. Zhou, J.; Zhao, M.; Wang, C.; Gao, Z. Optimal Design of Diversion Piers of Lateral Intake Pumping Station Based on Orthogonal Test. *Shock. Vib.* **2021**, *2021*, 6616456. [CrossRef]
29. He, Z.; Staples, G.; Ross, M.; Court, I.; Hazzard, K. Orthogonal Software Testing: Taguchi Methods in Software Unit and Subsystem Testing. *Logist. Inf. Manag.* **1997**, *10*, 189–194. [CrossRef]
30. Liang, Z.Z.; Tang, C.A.; Li, H.X.; Zhang, Y.B. Numerical Simulation of 3-D Failure Process in Heterogeneous Rocks. *Int. J. Rock. Mech. Min.* **2004**, *41*, 323–328. [CrossRef]

31. Tang, C.A. Numerical Simulation of Progressive Rock Failure and Associated Seismicity. *Int. J. Rock Mech. Min.* **1997**, *34*, 249–261. [CrossRef]
32. Li, G.; Lu, Z.; Xu, J. Regional Sensitivity Analysis of Aleatory and Epistemic Uncertainties on Failure Probability. *Mech. Syst. Signal. Process.* **2014**, *46*, 209–226. [CrossRef]
33. Li, G.; Xie, C.; Wei, F.; Wang, F. Moment-Independence Global Sensitivity Analysis for the System with Fuzzy Failure State and Its Kriging Method. *J. Syst. Eng. Electron.* **2018**, *29*, 658–666.